Development of a Plastic Scintillator-Based Active Shield for the ICARE-NG Radiation Monitor

Maxime Pinson, Pablo Caron, Philippe Laurent, Ion Cojocari

Development of a plastic scintillator-based active shield for the ICARE-NG radiation monitor

Maxime Pinson, Pablo Caron, Philippe Laurent , Ion Cojocari

***Abstract*—An active shield using a scintillator and silicon photo-multipliers (SiPMs) has been developed to operate with space environment particle detectors sensitive to both protons and electrons, such as ICARE-NG (Influence sur les Composants Avancés des Radiations de l'Espace-Nouvelle Génération). The method shows a reduction in electron contamination through the sides of the detector, thus increasing energy resolution. Two geometries are studied, one working in coincidence mode with the main detector, the other in anti-coincidence. Performances of both geometries are simulated in proton and electron environments in energy ranges typical of a space environment. Experimental measurements then aimed to validate the Monte-Carlo simulation framework for scintillating materials. Lastly, a case study of electron decontamination is carried out, as well as an error rate estimation in flux reconstruction.**

***Index Terms*—Monte-Carlo simulation, active shield, space physics, geometric factor, decontamination, veto counters, space environment measurements**

I. Introduction

MANY instruments have been flown in the past to measure the proton and electron population in the Earth's radiation belts, as well as galactic cosmic rays. To this end, several detectors such as the Relativistic Electron Proton Telescope (REPT) flown on the Radiation Belt Storm Probes (RBSP) in 2012, have been devised. The REPT uses a stack of silicon diodes in an aluminum casing [1].

Also, the RADMON detector [2] launched in 2017 uses a combination of a silicon detector and a CsI(Tl) scintillator for the detection of trapped protons and electrons.

Similarly, the ICARE-NG detector is composed of five silicon diode detectors arranged in three different casings labelled PE2S, PE1 and PE2. Fig. 1 shows a cutaway of a schematic version of one of the three heads of the ICARE-NG detector, head PE1. The diodes vary in thickness from 300 µm to 700 µm allowing for different energy detection ranges. The instrument has flown on several space missions, including SAC-C (2000), JASON-2 (2008) [3], SAC-D (2011) [4] and JASON-3 (2016).

Bigger instruments such as the Alpha Magnetic Spectrometer (AMS) installed on the ISS (International Space Station) in 2011, uses silicon strip detectors to reconstruct particle trajectories in its Silicon Tracker System [5]. The AMS also has an anti-coincidence counter (ACC) [6], designed to veto-out particles using plastic scintillators, wave-length shifting (WLS) fibers and photo-multiplier tubes (PMTs).

The solution studied here was to not use WLS fibers, and the small size of the detector led us to choose Silicon Photomultipliers (SiPMs) over PMTs due to their smaller size and growing commercial availability. Also, recent studies seem to highlight the higher photon detection efficiency of SiPMs over PMTs [7] making them a good candidate for our active shield.

Instruments such as REPT, RADMON, NGRM [8] and ICARE-NG use multi-channel analysers to sample energy deposits in the sensitive volumes (silicon diodes for the most part). The energy responses of these instruments depend greatly on the type of environment it is placed in, and is a superposition of all the types of particles encountered, mainly electrons and protons. A major hurdle in treating instrument data is the ability to separate the electron and proton contributions and convert the counts in the detector to proton and electron fluxes. One of the objectives of this paper is to try and overcome the difficulties associated with the counts to flux conversion in proton and electron environments.

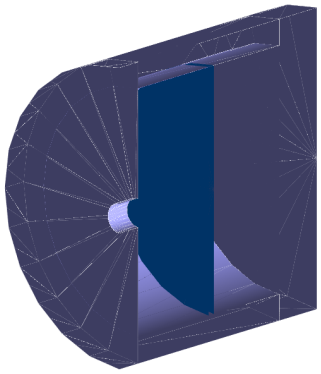

Fig. 1. Cutaway of the schematic geometry of the ICARE-NG detector head PE1 alone, on which the scintillator active shield is studied. A 3 mm radius hole is seen on the front of the aluminum casing. The rear side, which does not contain a hole, has the same thickness as the front : 5 mm.

The above cited instruments can all be subject to contamination by misidentified particles as well as high energy particles entering through the lateral aluminum shielding. The following work focuses on one geometry, that of ICARE-NG, to showcase the capabilities of an active shield and calculate the expected performance gain of the detector's measurements. This was made possible by coding end-to-end Monte Carlo simulations of the detector and scintillators.

M. Pinson is a PhD student with ONERA-DPHY Toulouse, France (e-mail: maxime.pinson@onera.fr), P. Caron is a research engineer at ONERA DPHY Toulouse, France (e-mail: pablo.caron@onera.fr), P. Laurent is a research engineer with CEA-IRFU Gif-sur-Yvette France (e-mail: philippe.laurent@cea.fr), and I. Cojocari is a PhD student with APC CEA Paris, France (e-mail: ion.cojocari@cea.fr)

Additionally, experimental studies carried out at ONERA were able to provide validation of the Monte-Carlo code used in this paper.

The most recent version of ICARE-NG (flown on Eutelsat E7C) is sensitive to protons and electrons in the typical kinetic energy ranges : 250 keV to 3 MeV for electrons and 30 to 350 MeV for protons. Specifically, the PE1 head of the instrument is composed of a single silicon diode with a thickness of 700 µm and a radius of 10 mm, encased in a 5 mm thick cylindrical aluminum case. This case has a small 3 mm diameter hole on the front. The following results focus on Monte-Carlo simulations of head PE1 alone because it is the only head containing a single diode, and has a small opening on the front. The other heads contain two diodes. This means that it can be subject to both the electron and proton environments simultaneously. Adding a scintillator and SiPMs can prove to be more cost efficient than adding a second diode for coincidence or anti-coincidence counting.

The diode detectors used are sensitive to an electrical charge created by the incident particle by ionization in the silicon. This electrical charge is proportional to the energy deposited by the incident particle. The ICARE-NG diode acquisition chain sorts the measured electrical charge into channels numbered from 0 to 127, where 127 corresponds to the highest deposited energy: approximately 3 MeV (or 23.5 keV per channel). The exact value of this energy is calculated during pre-flight calibrations.

One of the limits of the ICARE-NG instrument is the high energy electron contamination that occurs as these particles pass through the lateral aluminum shielding of the detector casing. These particles hit the diodes at grazing angles, whereas those passing through the front of the detector hit the diode almost perpendicularly, making their track lengths in the detector longer. This means that for a given incident energy, a particle entering through the sides is likely to deposit more energy than through the front of the detector. This leads to a higher variability in the detector response and reduces the energy resolution of the instrument.

To illustrate this, one can use the geometric factor (Gef), shown in Fig. 2, which is a quantity that expresses the proportion of particles that hit the diode detector out of all the particles simulated at that kinetic energy. The geometric factor is characteristic of the implemented geometry and of the nature of the incident particle, as it translates the effect of the geometry on particle collection in the diode. The geometric factor, G (in cm^2sr), can be defined as in [9] for a given incident kinetic energy by

$$G = \frac{n}{N} 4\pi^2 r^2 \tag{1}$$

where

- n number of detected particles by the diode
- N number of simulated particles at a given incident energy
- r radius of the sphere from which particles are initialized, in cm

The shapes of these geometric factors can be explained by the sub-atomic physics used in the GEANT4 simulation code.

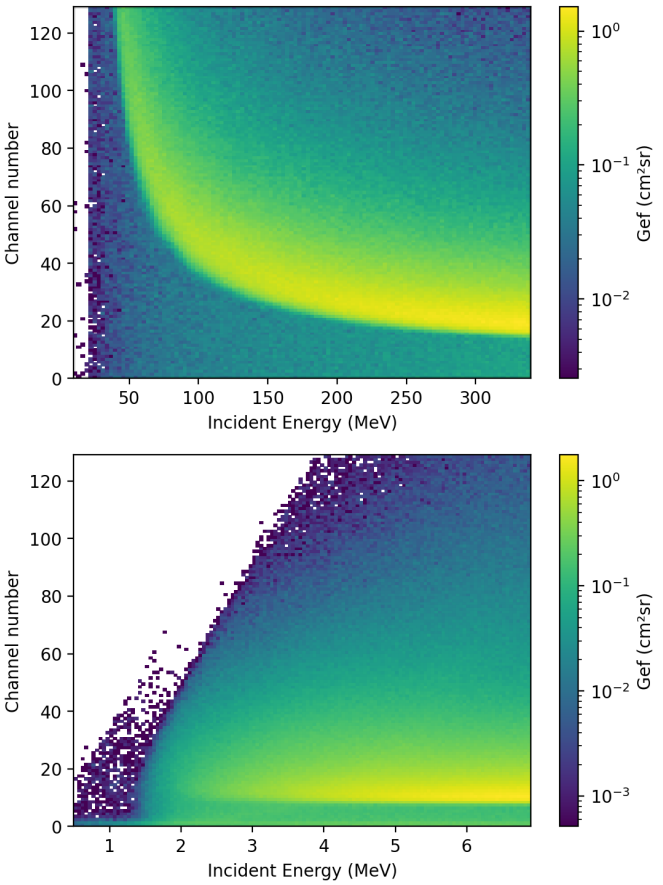

Fig. 2. Geometric factor (Gef) of head PE1 of ICARE-NG for protons (top) and electrons (bottom) in the energy range 10 MeV to 350 MeV and 0.5 MeV to 7 MeV respectively, without an active shield.

One notices that the proton geometric factor of Fig. 2 (top) is representative of the fact that the linear energy transfer (LET) is inversely proportional to its kinetic energy. The spread of the geometric factor around the main LET curve is due to protons arriving at non-perpendicular angles in the diode, which have a significantly longer track length in the silicon, depositing proportionally more energy. The geometric factor associated to the electrons, which are relativistic in this energy range, deposit an approximately constant amount of energy in the silicon diode. This minimum ionizing particle (MIP) behaviour which protons and electrons exhibit at high energies does not allow for the measurement of the kinetic energy by using the deposited energy in the diode.

Furthermore, electrons are subject to greater multiple scattering angles compared to protons, which are inversely proportional to the momentum of the particles. This greater scattering angle explains the difficulty in mitigating electron contamination in the detector. A low energy limit can also be seen in the electron Gef in Fig. 2 (bottom) due to the limited range of electrons at this energy and the aluminum casing of the detector head.

During a mission, information is gathered in the form of counts in the different channels (0 to 127). These counts can then be used to reconstruct the flux of the radiation belts using

the geometric factor of the instrument. An active shield would be able to modify the geometric factors of ICARE-NG in a way that would reduce the spread of the deposited energy, and thus improve its accuracy. In turn, these counts would give more precise information on the energies of the particles in the radiation belts, through the creation of differential channels for protons. This information would allow for the improvement of numerical models of the Earth's radiation belts which rely (partly of fully) on experimental data such as GREEN (Global Radiation Earth ENvironment) [10]. The geometric factors presented in Fig. 2 are shown as they are currently, without an active shield. By reducing the spread of these geometric factors, we can hope to dissociate both of these contributions.

II. Simulation setup

The simulations carried out here aimed to quantify the added-value of an active shield on head PE1 of the ICARE-NG instrument. These simulations used the GEANT4 simulation toolkit [11], as well as the GODDeSS [12] and G4SiPM [13] packages.

GEANT4 is a Monte-Carlo based code which relies on statistical and probabilistic methods to simulate the behaviour of sub-atomic particles in materials. The track of each particle is divided into a large number of steps, points at which random numbers are drawn by the simulation, which dictate the type of interaction that occurs. Within the GEANT4 framework, the GODDeSS package simulates the behavior of optical photon production for several different types of scintillators, and the G4SiPM package simulates the electrical response of an SiPM given optical photon stimulation. Along with the basic GEANT4 classes, these extra packages allow for an easier implementation of scintillators, fibers and SiPMs allowing for an end to end simulation of the active shield.

The simulated elements are the plastic scintillator (a BC-408 from *Saint Gobain*) and the Hamamatsu S10362-11-100U silicon photo-multiplier multi-pixel photon counter (MPPC). The BC-408 scintillator has a peak emission wavelength at 425 nm when ionized [14], with a yield reported to be around 10 000 photons/MeV [15], [16]. The Hamamatsu MPPC is composed of 100 square pixels with a width of 100 µm, which have a peak sensitivity (photon detection efficiency, PDE) of 65 % at around 440 nm. Both the fibers and the scintillator have relaxation times of a few nanoseconds, making them compatible for use in an anti-coincidence counter.

The electron and proton particle tracks are initialized isotropically from a sphere which encompasses the entire geometry in order to simulate a first approximation of a simple space environment.

III. Proposed geometries of the active shields

A. Scintillator and SiPM geometries

Two different active shield geometries were simulated in both electron and proton environments (Fig. 3). The first consists of a hollow cylindrical scintillator placed on the outside of head PE1 of the ICARE-NG instrument. The thickness of the diode was set to 300 µm.

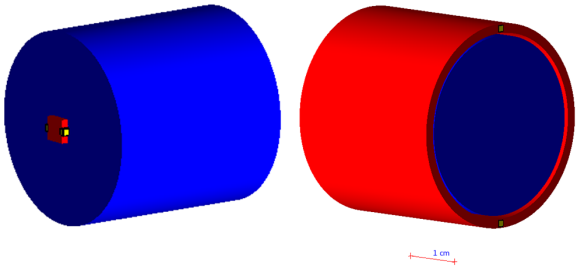

Fig. 3. The square (left) and cylindrical (right) geometries studied here. In blue, head PE1 of the ICARE-NG detector, and in red the scintillator material. The SiPMs can be seen in yellow glued to the scintillator material.

The radius of this cylinder is roughly that of the detector (1.5 cm), with a thickness of 0.5 mm. The scintillator must also be covered with a light-tight wrapping made of reflective material such as aluminum (teflon and Vikuiti can also be used) as to trap the photons within the material. Two SiPMs measuring 1 mm by 1 mm are glued to the surface of the scintillator, inside the wrapping.

The second geometry consists of a smaller, square piece of scintillator placed in front of the hole on head PE1. This piece is 3 mm wide and 0.5 mm thick. Similarly, two SiPMs are glued to the sides of the scintillator. This second geometry differs from the first in the sense that it works in coincidence mode, keeping only the particles that hit both the detector and the scintillator.

Several notable differences were found between these two solutions, both having some advantages and drawbacks, mainly because of their very different form-factors and the different counting modes used on each (coincidence/anti-coincidence).

B. Use of wave-length shifting (WLS) fibers

Several questions were raised as to whether or not the implementation of WLS fibers inside the scintillators would increase the overall detection efficiency. The role of the fibers is to guide the scintillation photons from the scintillator to the SiPMs which can thus be placed farther away from the scintillator. The fibers are encrusted into the plastic scintillator and one end of the fiber would face the sensitive surface of the SiPMs. This can prove to be useful in order to shield the SiPMs from radiation exposure. In both the cylindrical and the square geometries, the fibers were protruding from the scintillator material so that the SiPMs were 2 cm away from the scintillator. Results show that the use of WLS fibers have a negative effect on photon collection (Fig. 4), compared to a situation where the SiPMs are glued to the surface of the scintillator, as in Fig. 3. The number of photons collected on both SiPMs is reduced by a factor of about 8 for all incident proton energies. This reduced efficiency can be explained by the very small trapping efficiency of WLS fibers. On a more practical level, encrusting fibers inside plastic is quite costly and requires more equipment to make the setup light-tight.

Only a small proportion of the wavelength-shifted light is emitted at an angle that allows for total reflection inside the fiber. This value is said to be around 4 % depending on the type

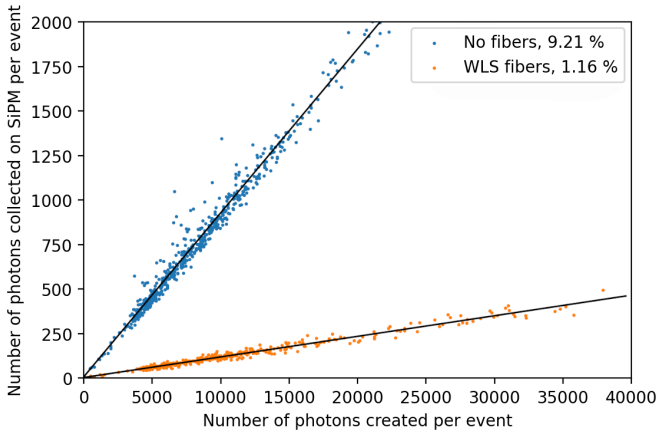

Fig. 4. Number of photons collected per event on the surface of the SiPM as a function of the number of photons created in the scintillator for 350 MeV protons. A factor of 8 between the collection efficiencies is noted.

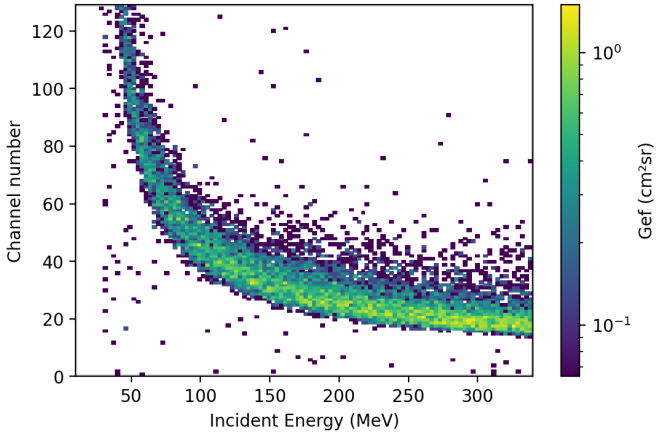

Fig. 5. Corrected geometric factor for the cylindrical scintillator geometry in a simulated proton environment with incident energies from 25 to 350 MeV

of fiber, for a numerical aperture of 0.74 [17]. Although the efficiency of the fibers is low, they still allow for a sufficient number of photons to be collected on the SiPMs for detection. This is especially interesting if the SiPMs need to be placed far from the instrument for electrical reasons and/or radiation exposure.

IV. Simulation Results and Discussion

The simulations were carried out in proton and electron environments separately in the energy ranges 10 MeV to 350 MeV and 500 keV to 7 MeV respectively. The geometric factors were calculated with and without the implementation of the active shield and serve as comparison.

To simulate the anti-coincidence counter, the optical photons are simulated from their creation in the scintillator all the way to their absorption by the SiPM. The electrical response of the SiPM is then simulated and if the peak of the electrical response is above 250 mV, the particle is considered as detected by the active shield. The 250 mV threshold was chosen as to avoid counting single cell pulses due to after-pulsing, cross-talk or thermal noise of the SiPM. The voltage range in which an SiPM is operational is quite narrow and is prone to drift with temperature and dose. In our simulations, the SiPMs were operated at 73 V, at an over-voltage of 1.5 V.

A. Cylindrical geometry

Final results of the cylindrical geometry show that an active shield can reduce the variability of the detector response and create differential modes for several different incident energy ranges for protons. Differential modes are groups of channels which are centered on a certain incident energy, giving information capable of reconstructing a differential flux. These differential modes start at around 50 MeV and can be seen up to approximately 100 MeV. Above this energy, the contributions from higher energy protons are too close to each other to obtain a clear separation. This can be seen on the geometric factor on Fig. 5 as the curve flattens at high energies.

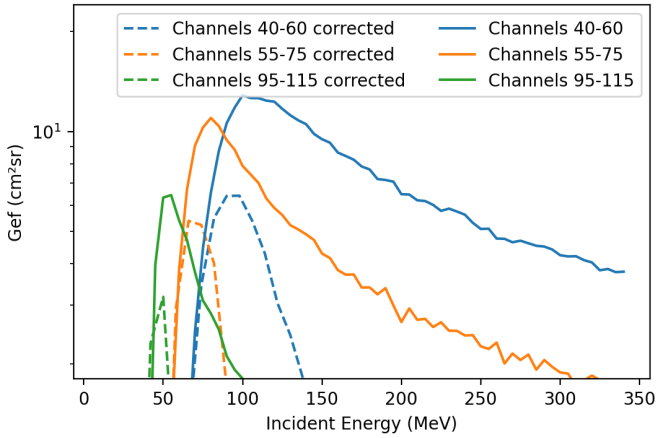

Fig. 6. Geometric factors as a function of incident energy on different groups of channels (from Fig. 5) for incident protons, before correction from Fig. 2 (solid lines) and after correction (dashed lines) by the cylindrical active shield. Differential channels can be seen at 50, 70 and 100 MeV for these different groups.

Examples of the obtained differential modes are shown on Fig. 6. These curves are horizontal cuts of the geometric factors for certain groups of channels of width 20. Above 200 MeV, integrated modes can be used to determine the contribution of protons with an energy above a certain threshold.

As for the electron environment with this geometry, results show only a minimal change in the number of electrons detected, Fig. 7, and thus does not solve the problem of electron contamination above channel number 20. The results suggest that many electrons are deflected at much greater angles by multiple scattering than the protons in the front and rear sides of the aluminum cover, as mentioned in I. In those cases, the scintillator fails to veto-out these electrons and the high energy contamination remains. These deflections mean that the angle of attack on the diode is not as significantly reduced as for protons. For electrons, the sharp increase in the geometric factor around 1.5 MeV (Fig. 2) is attributed to the greater penetration capabilities of higher energy electrons.

To eliminate this contribution, we need to be able to remove

all the counts that pass through the aluminum next to the hole on the front, as well as on the back of the cylinder. Placing another piece of scintillator on the back side of the detector head would not work because it would mean that we would need to distinguish particles using their time of flight to know which ones pass through the front (diode first and then scintillator) and the back (scintillator first and then diode), this aspect is not studied here. Another geometry has to be considered in order to eliminate the remaining contributions.

B. Square geometry

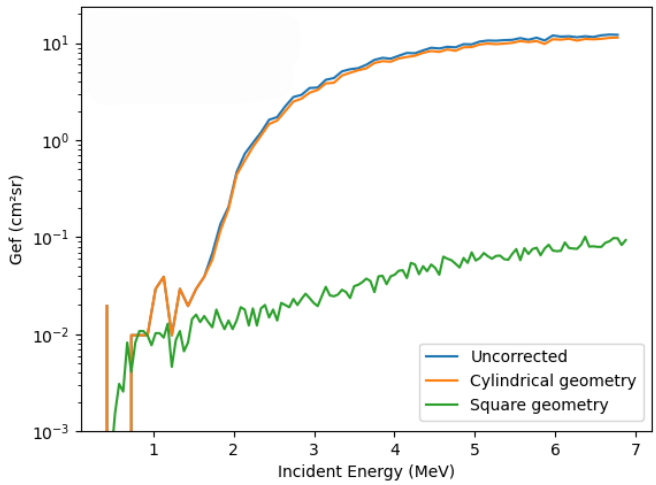

Fig. 7. Geometric factors as a function of incident energy for all channels from 9 to 127, before and after implementation of the square and cylindrical geometries. The rise in the geometric factor with electron energy is reduced by a factor of around 100 across the entire spectrum with the square geometry whereas the cylindrical geometry fails to reduce any high energy contamination.

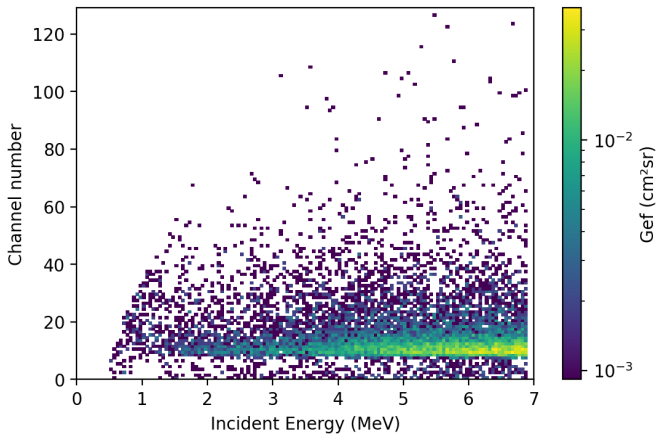

Fig. 8. Corrected geometric factor of the square scintillator geometry in an electron environment

The second (square) geometry aims to solve the problem of the electron environment while maintaining good performance for protons. The differential channels observed with the cylindrical geometry are conserved, and the associated Gef is not included due to its great resemblance to the cylindrical one (Fig. 5).

This geometry succeeds in reducing the number of electrons that pass through the aluminum covers, both front and back, due to its smaller form factor, Fig. 8. As a result, the increase in the geometric factor with incident energy is very limited and a significantly lower plateau can be observed at high energies. A significant advantage of this scintillator geometry is its ability to limit the electron response to lower channels. The square scintillator allows for decontamination above channel 20, which can be used for differential modes in the proton environment, as mentioned above.

V. Experimental validation of the Monte-Carlo simulations

A. Experimental setup

The experimental measurements carried out aimed to quantify the global performance of the Monte-Carlo simulations, for different types of radiation. The setup was devised to be able to characterize the energy spectrum of a ^{90}Sr $+^{90}$ Y electron source. This source has a 2.2 MeV spectrum end-point, requiring a long irradiation time to measure, which was not possible in our setup.

The experiments were carried out in a vacuum chamber and the read-out was ensured by a pulse shaper and an oscilloscope. The scintillating material was custom made to a thickness of 500 µm with a photon emission spectrum close to that of the BC-408. The SiPM used was a Hammamatsu 13360-6050CS. The scintillator was wrapped with one layer of Vikuiti reflector with optical glue. Several layers of Teflon are then added to ensure a light-tight wrapping. Only the SiPM wiring protrudes from the wrapping. Along the line of sight of the electron source, holes were made in the Teflon and Vikuti in both the front and back, to allow for the electrons to pass through the scintillating material and impinge the silicon diode as well. Otherwise, the range of the electrons was not sufficient for them to pass through the scintillator completely. Because of these holes, it is important for these experiments to be carried out in the total darkness, since the scintillator is no longer fully light-tight. The distance from the electron source to the scintillator was measured to be approximately 6.6 mm and scintillator to diode length was 4.3 mm and stayed the same through out the different experiments.

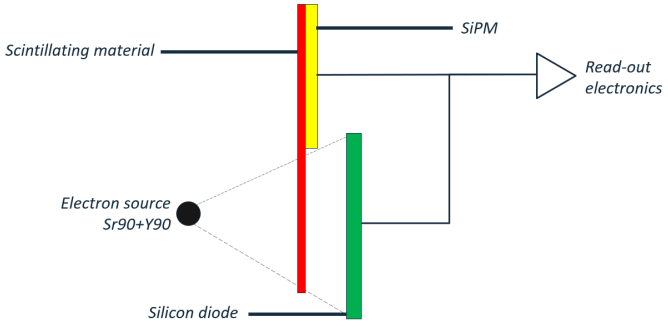

Fig. 9. Schematic of the experimental set-up with an electron source. The entire experiment (except for the read-out) was placed in a vacuum. The electron source was placed in such a way that it did not have a direct line of sight on the diode: it is entirely shadowed by the scintillator.

The silicon diode used was a Canberra PIPS detector of thickness 300 µm, the diode output was captured by a bias-T circuit which allowed for the polarization of the diode to -90 V all while sending the signal to a high-bandwidth current amplifier which delivers short current pulses (from 5 to 50 ns). This reversed polarization configuration allows for full depletion of the diode, maximizing the pulse height. The response was then amplified in a Canberra charge amplifier and read on an 8 GHz oscilloscope.

As for the SiPM, the over-voltage was set to 53 V and the signal was passed through an amplifier and then through a pulse shaper, which returns a short square signal of 100 ns. The activity of the electron source, which can be approximated by a point source, was 2.86 kBq. Being 6.6 mm away from the scintillator, the flux of the electron source was not high enough to cause any sort of pile-up in the SiPM nor diode.

The oscilloscope used has a sampling rate of 20 GS/s and is able to trigger based on pre-determined rules involving two different channels, allowing for a direct implementation of the coincidence counter.

B. $^{90}Sr +^{90} Y$ electron source measurements

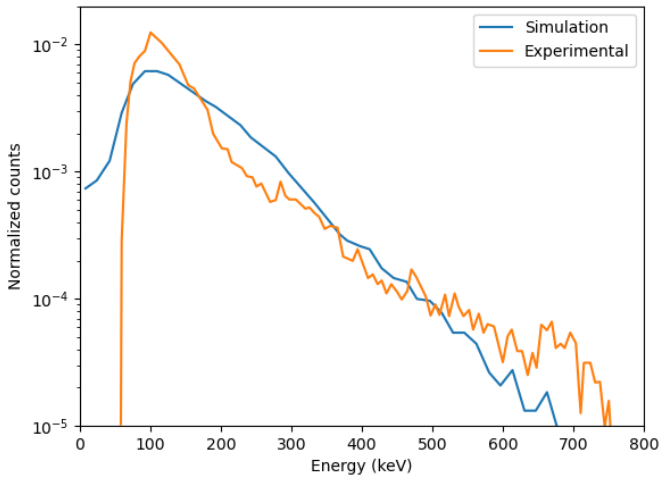

Fig. 10. Comparison of SiPM response of the simulated spectrum for the $^{90}Sr +^{90} Y$ electron source and experimental data

To implement a coincidence counter the $^{90}Sr+^{90}Y$ electron source was one of the only sources which could be used at ONERA since it is the only source that has a penetration length capable of passing through the entire depth of the scintillator. The other radioactive sources, all of which were alpha emitters, did not have sufficient ranges to impinge both the scintillator and the diode, rendering coincidence counting impossible. The experimental setup was implemented in GEANT4 using the same tool kits (GODDeSS and G4SiPM) as for the active shields. The energy spectrum gathered by the SiPM shows reasonable agreement with the predictions made by GEANT4 on Fig. 10. The experimental curves cut off at low energy (around 75 keV) due to the trigger height set by the oscilloscope.

In the same experiment, it was possible to implement a coincidence count of electrons passing through the scintillator and plotting the energy spectrum from the silicon diode. The simulated counts also show good agreement with the experimental data.

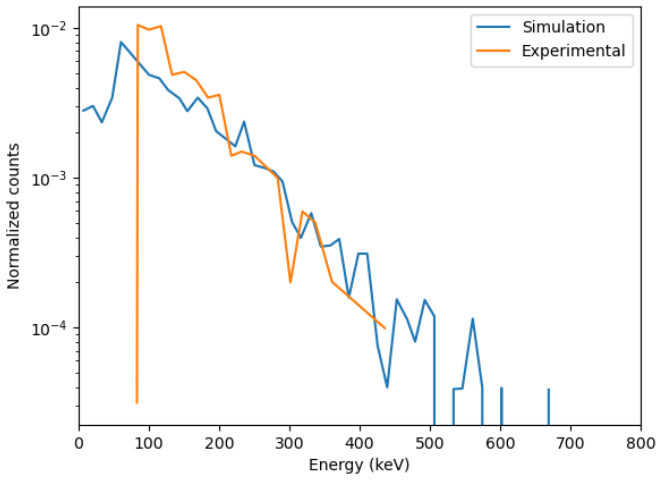

Fig. 11. Coincidence counts detected on diode with the $^{90}Sr +^{90} Y$ electron source only

VI. Added-value of the implementation of an active shield

A. Decontamination case study of a real space environment

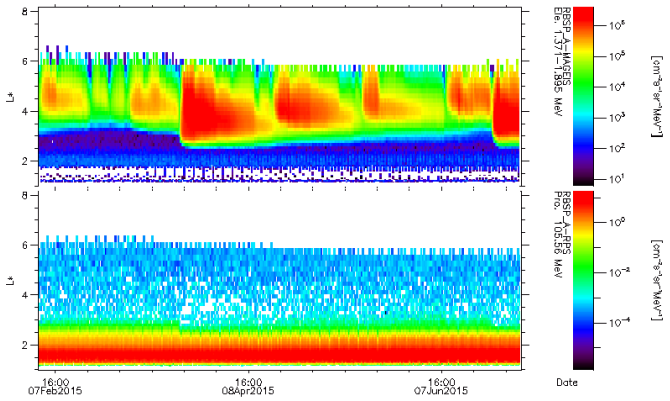

Fig. 12. Electron fluxes (top) and proton fluxes (bottom) in $cm^{-2}s^{-1}sr^{-1}MeV^{-1}$ for different L* values in 2015 over a 6 month period (February 2015 - July 2015) as measured by the RBSP-A MAGEIS and RPS instruments.

To show the efficiency of the square geometry in decontaminating the high-energy electron region, experimental data (Fig. 12) from the RBSP-A MAGEIS and RPS instruments is convoluted with the previously simulated geometric factors (both corrected and uncorrected) for protons and electrons, in Figs. 5, 8. This data measures proton flux at 105.56 MeV and electron flux between 1.371 MeV and 1.895 MeV. The result of the convolution is the number of counts per second detected by the simulated geometries had they been subjected to these fluxes of protons and electrons.

In the uncorrected case, the proton and electron fluxes cross around channel 95, which means that the channels below 95

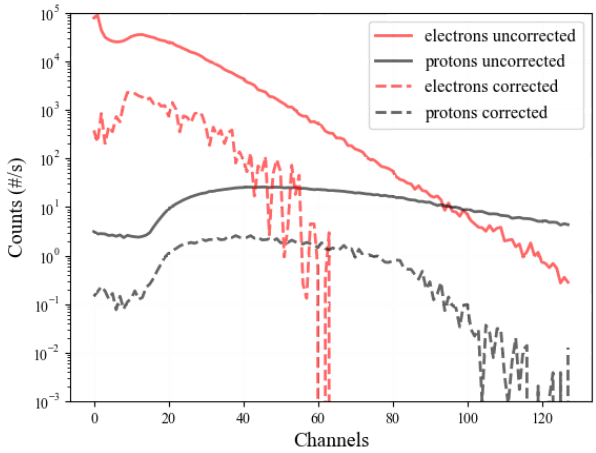

Fig. 13. Proton and electron counts in the different channels for corrected and uncorrected cases, for fluxes measured on 19/03/2015 by the RBSP-A MAGEIS and RPS instruments respectively. The channel to energy conversion is the same as for the previous geometries : 23.5 keV/channel.

are dominated by the electron flux, rendering the proton flux polluted. On the other hand, with the corrected version of the geometric factor, the proton/electron fluxes cross at channel 55, leaving all the channels above 55 free for differential proton flux modes as shown in Fig. 6.

B. Error reduction with differential channels in a proton environment

The differential channels created by the cylindrical geometry are more precise than those of the instrument without an active shield. This can be seen in Fig. 6 where the channels 40 to 60 are skewed towards the high energies in the uncorrected case. The cylindrical geometry reduces this problem since the Gef is centered more tightly and symmetrically around 95 MeV.

The method used here after aims to reconstruct a flux using the geometric factors of the corrected and uncorrected cases separately through a closure test. Using a chosen differential flux, we calculate the count rates in each channel by using the corresponding geometric factors. Then, using Gaussian approximations of the differential channels such as in Fig. 6, the flux can be partially reconstructed wherever these Gaussian approximations can be made. Finally, theses fluxes are compared to the original input flux.

This method uses a simplistic mathematical approach, which does not yield accurate results for the current geometries. Instead, more sophisticated methods are considered, such as singular value decomposition (SVD) [18], minimization [19] and artificial intelligence methods [20]. The fact that our geometric factors are cleaner than those of today's detectors allows us to justify the use of this simplistic inversion method.

For proton fluxes alone, the uncorrected case can be subjected to a higher error rate than the cylindrical geometry when calculating differential counts. If the proton flux were to be relatively flat in the 50 to 350 MeV range, then the channels 40 to 60 would be contaminated by the higher energy protons, due to the tail of geometric factor distribution in the uncorrected case in Fig. 6.

To show this, the proton flux f_p in $MeV^{-1}cm^{-2}sr^{-1}s^{-1}$ was modeled by an exponential power law such that:

$$f_p(E) \propto E^{\alpha} e^{\frac{-E}{\tau}} \tag{2}$$

with parameters α (unitless) and τ in MeV. This form was chosen because the (α, τ) parameter space covers a large variety of flux shapes.

The count rates C can be obtained by convoluting the flux f_p to the geometric factor matrices gef_p of the uncorrected and corrected cases (Figs. 2 and 5) by:

$$C(\alpha, \tau) = \int_0^{\infty} f_p(E) \text{gef}_p \, dE \tag{3}$$

as done in [18] and [21]. From these counts, one can isolate certain groups of channels in order to obtain differential fluxes centered on different incident energies, as demonstrated in Fig. 6. The reconstructed flux is then compared to the initial flux f_p.

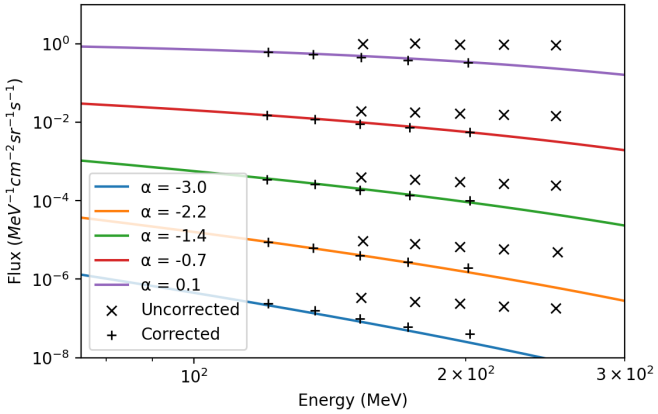

Fig. 14. Example of 5 different input fluxes with parameters τ = 125 MeV and different values of α. The reconstructed fluxes for differential channels between 100 and 250 MeV show good agreement with the corrected geometry whereas the uncorrected geometry significantly overshoots the real flux.

Fig. 14 shows an example of five different input fluxes and their reconstructions after using the corrected and uncorrected versions of the geometric factors of the cylindrical geometry. Each cross and plus sign represents a group of channels associated to a differential channel. The corrected geometry shows much better agreement with the input fluxes, which shows that differential flux reconstruction is easier with the implementation of an active shield.

Furthermore, the uncorrected geometry tends to consistently overestimate the input flux, this is because the differential channels associated to this geometry are skewed towards higher energies (Fig. 6) leading to higher energy particles being misinterpreted by the reconstruction as lower energy particles.

Given the variability of the proton flux shape in space, Fig. 15 represents the ratio of the mean relative error of the reconstructed flux compared to the original flux associated to a parameter pair (α, τ), which scans a wide range of flux shapes.

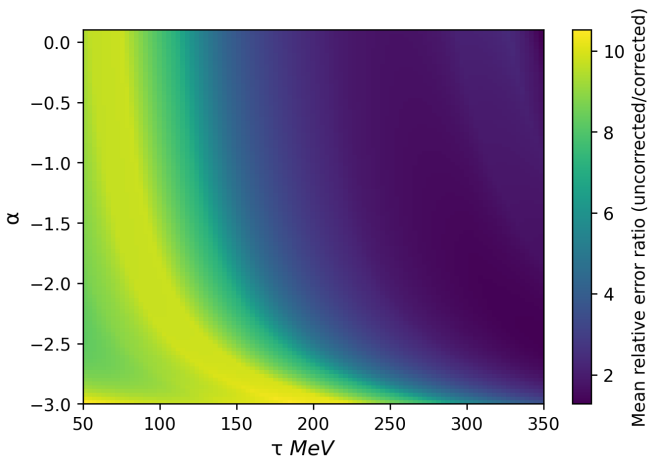

Fig. 15. Ratio of the mean relative error of five differential channels between the uncorrected and corrected cases for fluxes in the (α,τ) parameter space. In all fluxes shown here, the corrected cases error rate is lower than the uncorrected case.

VII. Conclusions

To conclude, this study has shown the type of performance improvements that we can expect from an active shield composed of a scintillator for the ICARE-NG space instrument. Such a shield on ICARE-NG would be able to reduce the angle of the particles hitting the diode, and can significantly improve the performance of the detector, as shown by the creation of differential modes for protons, and the electron decontamination above channel 20. Both of the geometries studied (cylindrical and square) manage to greatly modify and accentuate the geometric factors of the proton and electron environments. The main differences between the two geometries is the square geometry's ability to filter out high energy electrons while the cylindrical one does not. On the other hand, the square geometry reduces the total number of counts due to its much smaller form factor. Also, the experimental measurements have managed to validate the Monte-Carlo code that was used to simulate the generation and propagation of photons in scintillating materials.

References

[1] D. N. Baker, S. G. Kanekal, V. Hoxie, X. Li, A. N. Jaynes, H. Zhao, S. R. Elkington, J. C. Foster, R. Selesnick, B. Ni, H. Spence, and R. Filwett, "The Relativistic Electron-Proton Telescope (REPT) Investigation: Design, Operational Properties, and Science Highlights," *Space Sci. Rev.*, vol. 217, no. 5, Art No. 68, July 2021.

[2] P. Oleynik, R. Vainio, A. Punkkinen, O. Dudnik, J. Gieseler, H.-P. Hedman, H. Hietala, E. Hæggström, P. Niemelä, J. Peltonen, J. Praks, R. Punkkinen, T. Säntti, and E. Valtonen, "Calibration of RADMON Radiation Monitor Onboard Aalto-1 CubeSat," *Adv. Space Res.*, vol. 66, no. 1, pp. 42–51, July 2020. arXiv: 1911.07550.

[3] D. Boscher, S. A. Bourdarie, D. Falguere, D. Lazaro, P. Bourdoux, T. Baldran, G. Rolland, E. Lorfevre, and R. Ecoffet, "In Flight Measurements of Radiation Environment on Board the French Satellite JASON-2," *IEEE Trans. on Nucl. Sci.*, vol. 58 no. 3, pp. 916–922, June 2011.

[4] D. Boscher, T. Cayton, V. Maget, S. Bourdarie, D. Lazaro, T. Baldran, P. Bourdoux, E. Lorfevre, G. Rolland, and R. Ecoffet, "In-Flight Measurements of Radiation Environment on Board the Argentinean Satellite SAC-D," *IEEE Trans. on Nucl. Sci.*, vol. 61, no. 6, pp. 3395–3400, Dec. 2014.

[5] W. Burger, "The Alpha Magnetic Spectrometer Silicon Tracker," *Nucl Instrum. Methods A*, vol. 435, no. 1-2, pp. 886–891, Oct. 1999.

[6] P. von Doetinchem, W. Karpinski, T. Kirn, K. Luebelsmeyer, S. Schael, and M. Wlochal, "The AMS-02 Anticoincidence Counter," *Nucl. Phys. B - Proceedings Supplements*, vol. 197, no. 1, pp. 15–18, Dec. 2009.

[7] A. Hahn, A. Dettlaff, D. Fink, D. Mazin, R. Mirzoyan, and M. Teshima, "Results of the Parallel Operation of Large-Size SiPM Detector Modules and PMTs in IACTs," in *Proceedings of the 5th International Workshop on New Photon-Detectors (PD18)*, Art. No. 27 JPS Conference Proceedings, Journal of the Physical Society of Japan, Nov. 2019.

[8] L. Desorgher, W. Hajdas, I. Britvitch, K. Egli, X. Guo, Y. Luo, F. Chastellain, C. Pereira, R. Muff, D. Boscher, G. Maehlum, D. Meier, and P. Nieminen, "ESA Next Generation Radiation Monitor," in *2013 14th European Conference on Radiation and Its Effects on Components and Systems (RADECS)*, (Oxford, United Kingdom), pp. 23–27, IEEE, Sept. 2013.

[9] S. Pak, Y. Shin, J. Woo, and J. Seon, "A Numerical Method to Analyze Geometric Factors of a Space Particle Detector Relative to Omnidirectional Proton and Electron Fluxes," *Journal of the Korean Astronomical Society*, vol. 51, no. 4, pp. 111–117, Aug. 2018. arXiv: 1809.00123.

[10] A. Sicard, D. Boscher, S. Bourdarie, D. Lazaro, D. Standarovski, and R. Ecoffet, "GREEN: the new Global Radiation Earth ENvironment model (beta version)," *Annales Geophysicae*, vol. 36, pp. 953–967, 2018. Publisher: European Geosciences Union.

[11] S. Agostinelli *et al.*, "Geant4—a simulation toolkit," *Nucl Instrum. Methods A*, vol. 506, no. 3, pp. 250–303, July 2003.

[12] E. Dietz-Laursonn, T. Hebbeker, A. Künsken, M. Merschmeyer, S. Nieswand, and T. Niggemann, "GODDeSS: a Geant4 extension for easy modelling of optical detector components," *J. Instrum.*, vol. 12, no. 4, Art. No. 26, Apr. 2017.

[13] T. Niggemann, E. Dietz-Laursonn, T. Hebbeker, A. Künsken, M. Lauscher, and M. Merschmeyer, "G4SiPM: A novel silicon photomultiplier simulation package for Geant4," *Nucl Instrum. Methods A*, vol. 787, pp. 344–347, July 2015.

[14] Saint-Gobain, "BC-408, BC-412, BC-416, solid plastic and liquid scintillation materials, Saint-Gobain Crystals." [Online] Available : https://www.crystals.saint-gobain.com/products/bc-408-bc-412-bc-416.

[15] R. Ogawara and M. Ishikawa, "Signal pulse emulation for scintillation detectors using Geant4 Monte Carlo with light tracking simulation," *Rev. Sci. Instrum.*, vol. 87, no. 7, Art. No. 075114, 2016.

[16] S. Riggi, P. La Rocca, E. Leonora, D. Lo Presti, G. Pappalardo, F. Riggi, and G. Russo, "Geant4 simulation of plastic scintillator strips with embedded optical fibers for a prototype of tomographic system," *Nucl Instrum. Methods A*, vol. 624, no. 3, pp. 583–590, Dec. 2010.

[17] Saint-Gobain, "Scintillating fibers Saint-Gobain Crystals." [Online] Available : https://www.crystals.saint-gobain.com/products/scintillating-fiber.

[18] V. Maget, S. Bourdarie, D. Lazaro, D. Boscher, G. Rolland, R. Ecoffet, and E. Lorfevre, "Unfolding JASON-2/ICARE-NG High-Energy Particles Measurements Using a Singular Value Decomposition Approach," *IEEE Trans. on Nucl. Sci.*, vol. 61, no. 4-1, pp. 1687–1694, Aug. 2014.

[19] M. Matzke, "Unfolding procedures," *Radiat. Prot. Dosim.*, vol. 107, no. 1-3, pp. 155–174, Nov. 2003.

[20] S. Aminalragia-Giamini, C. Papadimitriou, I. Sandberg, A. Tsigkanos, P. Jiggens, H. Evans, D. Rodgers, and I. A. Daglis, "Artificial intelligence unfolding for space radiation monitor data," *J. Space Weather Space Clim.*, vol. 8 Art. No. 50, 2018.

[21] I. Sandberg, I. A. Daglis, A. Anastasiadis, P. Buhler, P. Nieminen, and H. Evans, "Unfolding and Validation of SREM Fluxes," *IEEE Trans. on Nucl. Sci.*, vol. 59, no. 4, pp. 1105–1112, Aug. 2012.